LANGMUIR

pubs.acs.org/Langmuir Article

Characterization of Surface Patterning on Polymer-Grafted Nanocubes Using Atomic Force Microscopy and Force Volume Mapping

Wade Shipley, Yufei Wang, Joelle Chien, Bin Wang, and Andrea R. Tao*



Cite This: Langmuir 2024, 40, 20464-20473



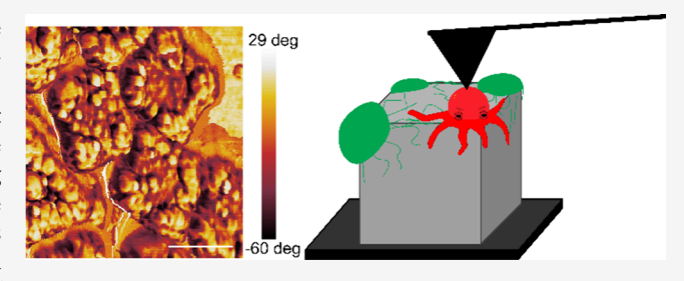
ACCESS I

Metrics & More

Article Recommendations

Supporting Information

ABSTRACT: Atomic force microscopy (AFM), in particular force spectroscopy, is a powerful tool for understanding the supramolecular structures associated with polymers grafted to surfaces, especially in regimes of low polymer density where different morphological structures are expected. In this study, we utilize force volume mapping to characterize the nanoscale surfaces of Ag nanocubes (AgNCs) grafted with a monolayer of polyethylene glycol (PEG) chains. Spatially resolved force—distance curves taken for a single AgNC were used to map surface properties, such as adhesion energy and deformation. We confirm the presence of



surface octopus micelles that are localized on the corners of the AgNC, using force curves to resolve structural differences between the micelle "bodies" and "legs". Furthermore, we observe unique features of this system including a polymer corona stemming from AgNC—substrate interactions and polymer bridging stemming from particle—particle interactions.

■ INTRODUCTION

Patchy nanoparticles (NPs), i.e., NPs that possess at least one region of distinctly different surface chemistry from the rest of the NP, are a promising class of materials that have the potential to impact a variety of applications where multicomponent or multipurpose nanostructures are required. This includes drug delivery, where patchiness allows for storage of drug cargo, tailored solubility, and cellular uptake, ^{1–3} as well as heterogeneous catalysis, where patchiness simultaneously enables reactions to catalytically active surfaces and colloidal stabilization. ^{4,5} Patchy NPs can also serve as a foundational building block for self-assembly ^{6–9} and as templates for the synthesis of complex multicomponent NPs, where patches of low ligand density or specific chemical functionality allow for the nucleation of a secondary material. ¹⁰

Grafting a NP surface with polymers is a common strategy for generating patchiness, since both polymer composition and surface distribution can impart chemical anisotropy to the NP surface. While a large body of work has been developed on the fabrication of patchy NPs whose surfaces are ligated with multiple types of polymers ^{11–13} or with grafts that preferentially self-segregate, ^{14,15} recent work has demonstrated that patchiness can also arise in NPs ligated with a single type of polymer graft without any intentional anisotropy in macromolecular structure or graft chemistry. For example, polymergrafted NPs that are dispersed in poor solvents ^{16,17} (i.e., where chains are more strongly attracted to themselves than the solvent) or dried in air ¹⁸ have been observed to exhibit patchy graft layers where the graft chains condense into nanoscale

regions of uneven chain density. These patches are typically described as octopus micelles $^{19-21}$ or surface-pinned micelles. $^{16,17,22-24}$ They consist of a core of dense, collapsed polymer that connect to the grafting surface via stretched chains, resembling an octopus with outstretched legs. These micelles form in regions of intermediate grafting density where grafted chains favor interactions with other chains (i.e., instead of solvent) while balancing the entropic penalty of chain stretching. 20 The number and size of these micelle regions is highly dependent on the ratio of NP diameter to the radius of gyration (R_{σ}) of the grafts.¹⁸ In addition, shaped NPs, such as nanorods, triangular nanoprisms, and nanocubes, dried out of a poor solvent possess octopus micelles that are localized near the edges and corners of the NP (i.e., high curvature regions with higher graft density). 16,17 While computer simulations and theoretical methods have provided insights into the structure and formation mechanism of octopus micelles, experimental studies have been limited to direct imaging by transmission electron microscopy, which is only able to resolve the densest patches of polymer and is unable to provide characterization of graft conformations 16,17 or regions with lower graft densities, such as the micelle legs where polymer

Received: May 20, 2024
Revised: August 29, 2024
Accepted: September 5, 2024
Published: September 19, 2024





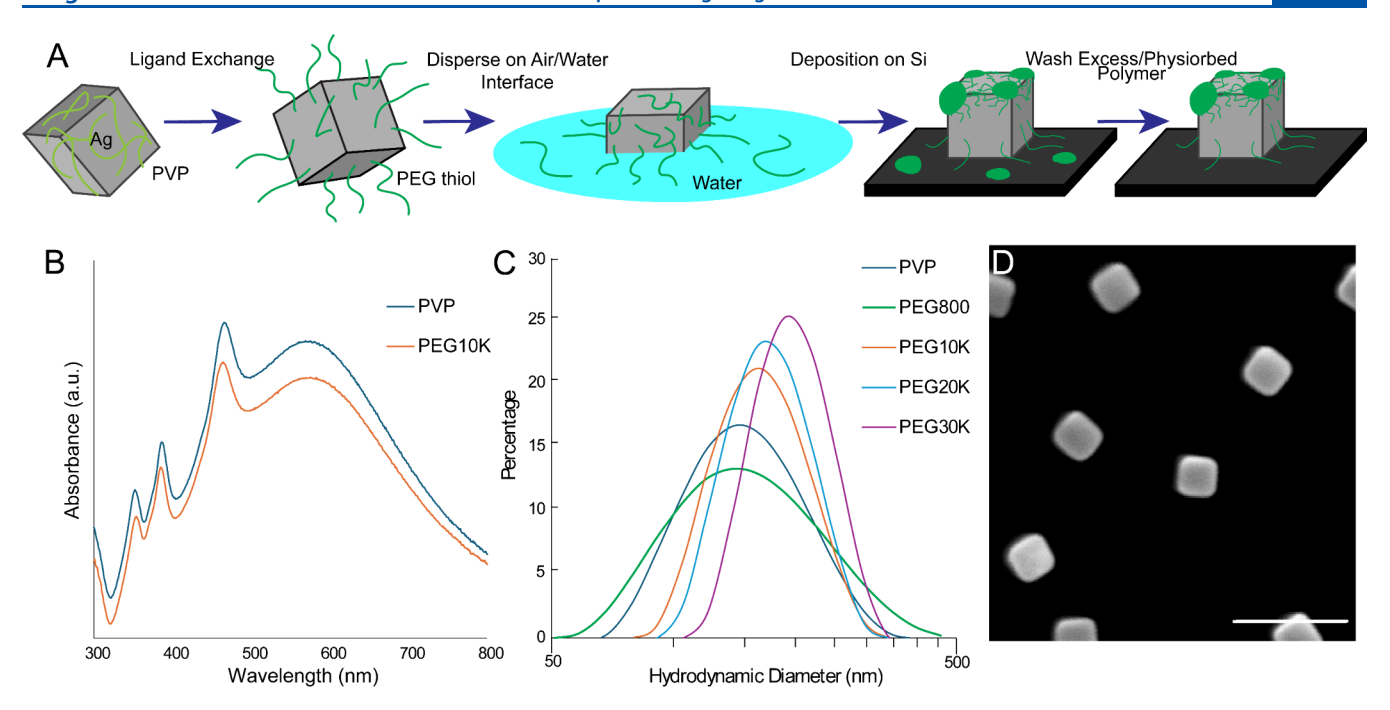


Figure 1. Sample preparation for AFM experiments. (A) AgNCs are PEGylated, suspended on an air—water interface, dip-coated onto a Si substrate, then washed and dried for AFM measurements. (B) Ultraviolet—visible (UV—vis) absorbance spectra of PVP-grafted and PEG10K-grafted AgNCs. (C) Dynamic light scattering number distribution plots showing changes of hydrodynamic diameter with increasing PEG chain length. (D) Scanning electron microscopy (SEM) image showing AgNC grafted with PEG20K. Scale bar is 200 nm.

chains are stretched inward toward the more dense octopus "body". 18

Atomic force microscopy (AFM) is a widely used tool for the characterization of polymer grafts, ²⁵⁻²⁸ with the potential to provide such insights for polymer-grafted patchy NPs with nanometer-level spatial resolution. For example, standard AFM topography images can reveal conformational transitions in grafted polymers between pancake, mushroom, micelle, or brush states in air or a variety of solvents, 19,26,27,29 along with the heights of the brushes. 27,28,30,31 AFM-based force—distance curves, where the AFM tip travels a given distance into the sample surface and the tip-sample forces are measured, allow for nanoindentation measurements where modulus or grafting density is determined^{27,28,32,33} or for pulling of single polymer molecules, 34-37 both of which can provide insights into polymer structure. While individual force spectroscopy curves can provide many details about a surface, spatially resolved force measurements are necessary for elucidating the macromolecular properties of polymer-grafted NPs and to characterize the formation of polymer patches on the NP surface. Recently, Lemoine et al. 38 utilized force spectroscopy to characterize the polymer packing for polyethylene glycol (PEG)-grafted spherical Au NPs utilized in drug delivery applications. However, they found that their measurements were inconclusive for NP surfaces with low grafting densities when analyzing single force-distance curves collected from different locations on the NPs, likely due to inhomogeneities associated with the polymer-grafted surface. In contrast, force volume mapping takes a point-by-point array of force spectroscopy measurements to provide quantitative, spatially resolved information regarding surface properties, such as adhesion or stiffness. 39-41 The lateral resolution of the resulting force map is limited by the size of the AFM tip (often in the 5-25 nm range) allowing surface property variations to be visible on the nanoscale. This high spatial

resolution is sufficiently high for revealing surface properties of single NPs that might be otherwise unmeasurable by standard AFM topography, such as nanoscale differences in compressibility. 42,43

Here, we demonstrate force volume mapping and AFM imaging of polymer-grafted AgNCs with different grafting chemistries, graft sizes, and graft densities to characterize the nature of the polymer graft layer, including the formation of dense polymer patches and octopus micelles. AgNCs were used as the NP core because they have flat facets and low surface roughness, which provides a model NP system for analyzing surface structures. In particular, we characterize AgNCs grafted with a thiolated PEG chain, which was previously reported to possess PEG grafts that are evenly distributed over the entire AgNC surface.⁴⁴ We demonstrate that force volume maps can be obtained for the surface of a single PEGylated AgNC, revealing contrast in polymer conformation and behavior across low- and high-density regions. This polymer density contrast is only observed for grafts with sufficient chain length and mobility that can enable large regions of stretched polymer.

■ RESULTS AND DISCUSSION

Figure 1A shows a schematic of the sample preparation for force volume mapping measurements. AgNCs were synthesized via a previously reported polyol method⁴⁵ resulting in as made nanocubes grafted with the native capping ligand, polyvinylpyrrolidone (PVP). The nanocubes were either PEGylated with a thiolated PEG chain using various molecular weights, ranging from 800 Da to 30 kDa, or grafted with a thiolated polystyrene (PS) chain with molecular weights of either 11 or 50 kDa. To carry out force volume mapping, the AgNCs were dispersed in chloroform and suspended on an air—water interface before being dip-coated on a Si substrate as previously described. 46,47 AFM maps were obtained after

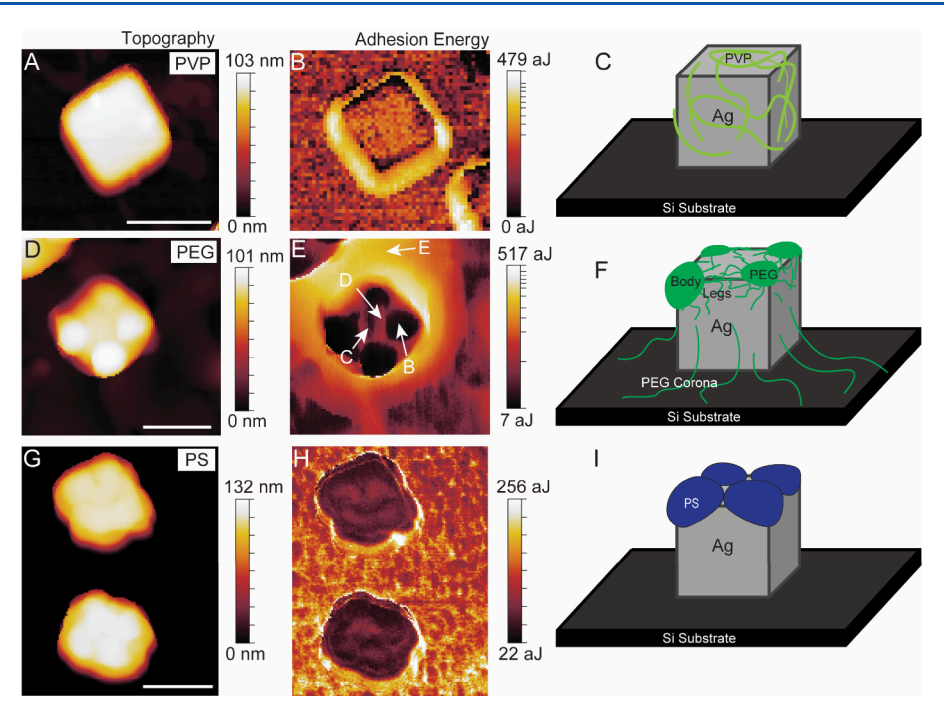


Figure 2. Force volume mapping results. Each pixel represents a force curve, with a set point of 6 nN and a pixel size of 3–4 nm². Scale bar equals 100 nm for all images. (A) Amplitude modulation topography image output of the height for the as prepared PVP AgNC. (B) Calculated adhesion energy from force mapping at a force set point of 6 nN for the same PVP AgNC. A smaller cuboctahedron particle was pushed into the bottom right corner. Areas of high adhesion energy surrounding the particle are artifacts of the AFM tip dragging along the nanocube sidewalls. (C) Schematic showing the expected polymer conformation of the nanocube, with PVP evenly coating the surface. (D) Height image of PEG10K grafted AgNC. (E) Adhesion energy image. Noticeable variations across the surface are visible. A ring of higher values forms a corona around the nanocube extending beyond the regions caused by AFM tip dragging. (F) Schematic of the expected polymer conformation. Dense clusters of polymer are raised in the topography image and have low adhesion, the stretched chains extending from the clusters have higher adhesion. (G) Topography image of PS50K grafted AgNC. (H) Adhesion energy image showing micelles with low adhesion energy across most of the nanocube surface. (I) Schematic showing large micelles covering most of the top face.

drying the deposited AgNCs in a vacuum desiccator until completely dry, rinsing the sample under deionized water for 1 min to remove any remaining physisorbed polymer, and drying in a vacuum desiccator for an additional 2 h. We then acquired standard amplitude modulation mode topography and phase images to find regions of interest and assess the uniformity of the sample. We then obtained force maps where each pixel corresponds to a single force—distance curve between the AFM tip and sample. Analysis of these force curves provides a wealth of information regarding the surface properties of the polymer-grafted AgNCs and allows the identification of unique surface patches or regions based on these properties.

Three different surface chemistries were initially examined, starting with the as-synthesized PVP-grafted AgNCs, followed by AgNCs grafted with PEG-thiol with a $M_{\rm w}$ = 10 kDa (PEG10K) and AgNCs grafted with PS-thiol with $M_{\rm w} = 50$ kDa (PS50K). Figure 2A shows the topography from amplitude modulation and Figure 2B shows the adhesion energy from a force volume map with a force set point of 6 nN obtained for a single PVP-grafted AgNC. The adhesion energy values were defined as the integral of the retraction curve below zero. The topography image shows some small clusters on the AgNC surface that are likely chains of PVP that have coiled together (based on their lower adhesion energy values), though a thinner, more extended layer still covers the nanocube facet.⁴⁸ (section S.1 of the Supporting Information for the corresponding phase image). In the adhesion energy image, a smaller defect NP was pushed into the bottom right corner of the image and a large cluster of polymer is visible on

the substrate in the top right corner (section S.2 of the Supporting Information). The AgNC shows higher values of adhesion along the sides, which is an artifact from the AFM tip dragging along the sidewalls resulting in an increased contact area. Figure 2C shows the expected conformation of PVP, corresponding to polymer chains that are anchored at multiple chain sites. 48

Panels D and E of Figure 2 show the topography and adhesion images for an AgNC grafted with PEG10K. A second AgNC is visible in the top left corner in both images. We observe raised circular bumps located in each facet corner, indicative of large polymer clusters consistent with the surface patterning observed by Gallati due to the formation of octopus micelles. ¹⁷ The bumps are raised approximately 8–12 nm from the AgNC surface, though the smallest bump (top corner) is raised only ≈1 nm. In Figure 2E, the PEGylated AgNC shows a lower adhesion energy on the facet corners directly on top of the raised bumps (region B, 20.2 ± 6.5 aJ, averaged) and in the facet center (region C, 38.9 ± 1.5 aJ). A higher adhesion energy is observed for the remaining area of the AgNC facet (region D, 52.4 ± 4.4 aJ), excluding the center and micelle regions, as well as for a corona-like region surrounding the outer perimeter of the AgNC (region E, 124.8 \pm 61.4 aJ). Figure 2F shows a schematic of these various regions and the expected conformation of PEG10K with respect to the AgNC. Our measurements are consistent with predictions that the polymer chains on the AgNC face will stretch toward higher polymer density regions on the AgNC edges and corners, 17 creating the octopus micelle "body" (i.e., the center of the

observed bumps) and the stretched "leg" regions. Our AFM measurements show the clear variation in adhesion energy between these two regions: dense polymer clusters have a low adhesion energy, extended polymer chains have a high adhesion energy. This is also consistent with the high adhesion energies in the corona region, where we observe polymer grafts to possess a strong affinity for the substrate. ¹⁸

Panels G–I of Figure 2 show the results for PS50K-grafted AgNCs. The topography image in Figure 2G shows the presence of four large micelles on the top face of both AgNCs in the image, where the micelles are centered on the corners and slightly overlapping. PS micelles are also observed on the AgNC sidewalls, consistent with previously reported TEM images of PS-grafted Au nanocubes. 16,17 The adhesion energy map in Figure 2H shows low adhesion energy values (69.0 \pm 13.5 aJ) and limited contrast, indicating the formation of a dense layer graft layer on the AgNC surface. Adhesion energy maps of AgNCs grafted with shorter PS chains (e.g., PS11K) show similar micelle formation with greater contrast, attributed to the shorter chains and smaller micelles (section S.3 of the Supporting Information).

Figure 3 shows high-resolution amplitude modulation images for PEGylated AgNCs grafted with various PEG molecular weights. As the chain length increases, large octopus micelles form at the AgNC corners. For PEG20K-grafted AgNCs, the phase image in Figure 3A shows large, lumpy micelles forming primarily on the AgNC corners, as well as on

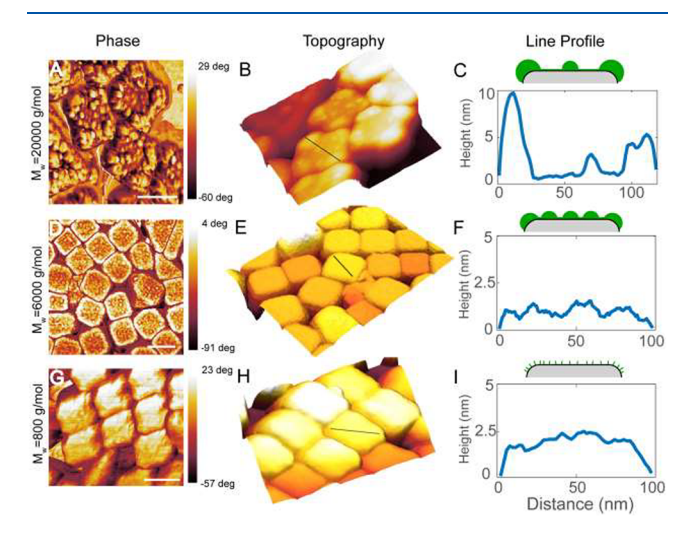


Figure 3. Amplitude modulation images showing the variation in nanocube surface morphology with length of the grafted polymer PEG thiol. Scale bar equals 100 nm for all images. Panels A-C show the results for PEG20K. The phase image shows large micelles of polymer on the nanocube corners with smaller micelles on the faces and edges. A large nanotriangle is visible in the bottom left corner also showing micelle formation. The topography image shows the micelles are raised above the surface of the nanocube along with the line profile, taken from corner to corner indicated in the topography images. Panels D-F show the results for PEG6K. The phase image shows many smaller clusters on the surface, which is also shown in the topography image. The line profile from corner to corner gives the heights of the clusters, which are small and in the 0.5 to 1 nm range. Panels G-I show the results for the shortest length PEG800. The phase image resolves an even surface with some slight undulations. The topography and line profile show a surface with slight roughness and curvature. No clear clustering, pattern or micelle formation is observed.

the AgNC edges. The centers of the AgNC faces are generally flat and smooth, with the appearance of some much smaller micelles. The topography image in Figure 3B and the line profile in Figure 3C show that the large corner micelles are raised by 5-10 nm while the smaller micelles located in the face center are only 2-4 nm high. Panels D-F of Figure 3 show the corresponding AFM data for PEG6K-grafted AgNCs, where the octopus micelles appear as prominent clusters (i.e., high contrast) on the AgNC surface with heights from 0.5 to 1.5 nm. Given that the expected random walk radius in air for PEG6K is 4 nm⁴⁹ is notably larger than the cluster heights, it suggests the grafts are in the brush regime as expected. 50,51 It is possible that the PEG6K chains are not sufficiently long to stretch and form larger, more energetically favorable micelles, 20 or that the shorter chains do not form a sufficient grafting density gradient on edges and corners.¹⁷ Along these lines, panels G-I of Figure 3 show the AFM data for AgNCs grafted with PEG800 that confirms that these shorter graft lengths result in a decrease in the size and appearance of polymer clustering. Both the phase image and line profile do not show any clear micelle formation or surface pattern. A slight curvature is visible on all the nanocube faces.

To provide more detailed characterization of octopus micelle formation for PEGylated AgNCs, we examined representative force curves for several regions obtained from the force volume map in Figure 2E. Each curve was taken from the labeled regions in Figure 2E, and a representative PEG 10K AgNC was selected (section S.4 of the Supporting Information). Figure 4A shows a schematic of the force measurement, with key distances (d) labeled during approach and pull-off events. All distances given are relative to the max force value, at d = 0. As the AFM tip approaches the sample, the surface capillary layer will neck outward and the tip begins to undergo a dynamic snap-in process. We assume the surface capillary layer does not neck outward from the surface to the AFM tip to a substantial degree given the sharp nature of our AFM tips (nominal: r < 7 nm, deconvoluted: r < 5 nm). The onset of the snap-in process begins at $d_{\rm On}$. The region between $d_{\rm On}$ and $d_{\rm Sur}$ is the continuation of the snap-in process and this total length can be used as an approximation of the liquid film thickness on surfaces. 52-54 Additional forces curves taken as single spectra at a slower rate are shown in section S.5 of the Supporting Information.

The contact point is assumed to be at the minimum force value and given as d_{Sur} . SS,S6 Deformation occurs during loading between d_{Sur} and the max force of 6 nN. As the AFM tip pulls away, the surface layer of water and polymer chains can form bridges between the tip and the sample before completely breaking off at $d_{\rm Off}$. S5,57,58 This polymer bridging is apparent when comparing the pulloff behavior for different PEG chain lengths, which scales with graft chain length (section S.6 of the Supporting Information). Panels B-E of Figure 4 show representative force curves from each labeled region in Figure 2E and are randomly selected from areas without a high likelihood of tip artifacts (section S.7 of the Supporting Information): the micelle body (Figure 4B), the AgNC face center (Figure 4C), the micelle legs (Figure 4D), and the corona region (Figure 4E). All curves show bridging on the retraction, but the micelle legs and corona region have notably longer bridging (25.0 and 73.2 nm respectively), which indicates lower chain density and more mobile chains that can be pulled further by the AFM tip. 51,57 Furthermore, these regions likely have a thicker liquid surface layer due to the

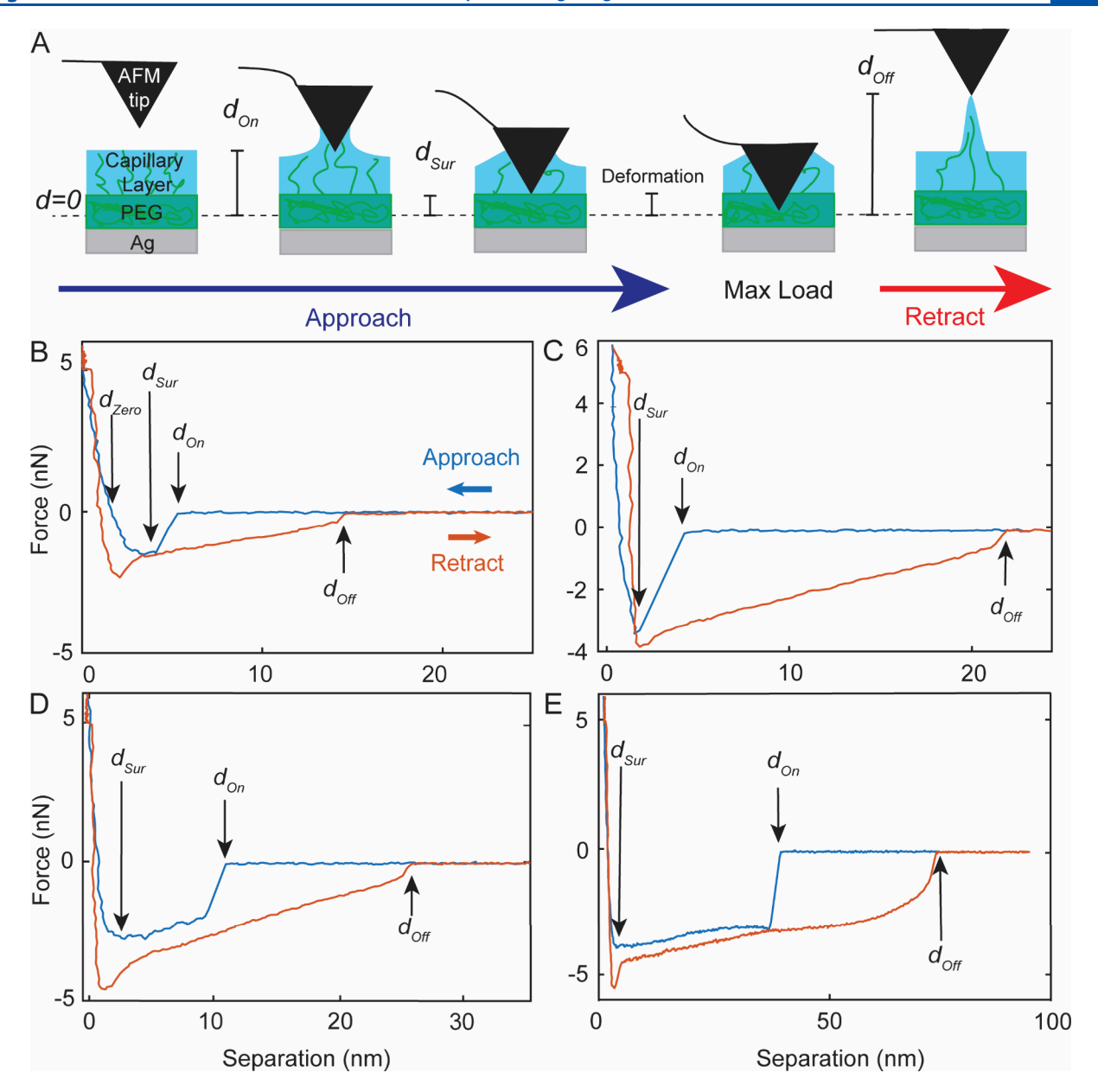


Figure 4. Analysis of the force curves showing representative force separation curves randomly selected from the force volume map for each region. Locations are given in adhesion energy image by arrows in Figure 2E. (A) Schematic showing the expected behavior between the AFM tip and the polymer-coated AgNC surface in ambient air. Some swelling of the brush is expected due to water vapor. The surface capillary layer pulls the tip in at point $d_{\rm On}$ then reaches the denser polymer surface at $d_{\rm Sur}$. A load is applied and some deformation of the polymer occurs until a max load is reached, then the tip is pulled away, pulling some polymer molecules and forming a capillary bridge. (B) Octopus micelle body. (C) Nanocube center. (D) Octopus micelle legs. (E) Corona. Some nonlinearity exists in the curves due to overshoot.

longer snap-in length, suggesting more vapor swelling due to their lower densities $^{59-61}$ along with some changes in polymer structure during the snap-in process specific to the leg regions. 51 In comparison, the micelle body and nanocube center show smaller snap-in lengths and while there is some bridging on retraction, it is shorter (13.5 and 19.7 nm, respectively). The micelle body shows some deformation (1.5 nm using $d_{\rm Zero}$ as the contact point and 3.8 nm using $d_{\rm Sur}$), consistent with a dense cluster of soft polymer. The force curve for the AgNC face center suggests that this region is characterized by the presence of very little polymer, and the grafts that are present are likely highly stretched toward regions of higher polymer density (i.e., clusters at the edges, corners). For comparison, a representative force separation curve from a

clean silicon surface is shown in section S.8 of the Supporting Information.

Panels A–C of Figure 5 show the corresponding property maps of the calculated pull-off length (the distance of the attractive bridging on the retraction curve), deformation (using $d_{\rm Zero}$ as the contact point for simplicity⁶²), and the snap-in distance (distance of the attractive plateau after $d_{\rm On}$) for the curves obtained from the force volume map shownin Figure 2E. Additionally, snap-in force and adhesive force are included in section S.9 of the Supporting Information. Each map is 100 × 100 pixels and comprised of 10 000 force curves. Figure 5D shows a color-coded schematic of the various regions defined in Figure 2E along with the number of force curves included in the analysis of each region (section S.10 of the Supporting

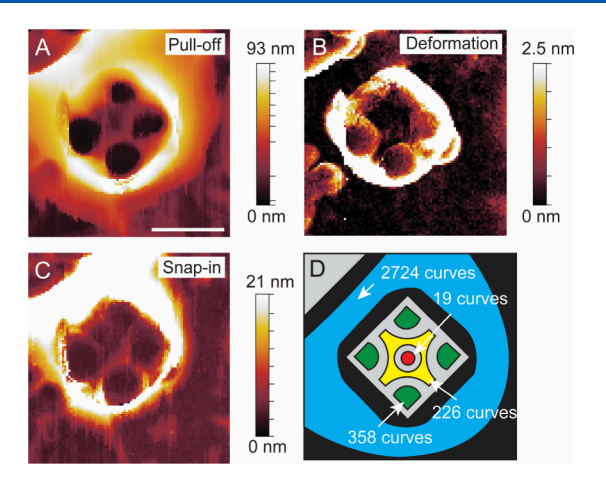


Figure 5. Maps of different calculated parameters made from force volume maps, with each pixel corresponding to a force curve, with a total of 10 000 pixels. Scale bar corresponds to a length of 100 nm. (A) Pull-off of each retraction curve showing variation of bridging length of the AFM tip and sample surface. Lower values are found on the corners and in the center. A corona of higher values is also visible. Color map is with adaptive color scaling and each tick corresponds to 9 nm. (B) Deformation image showing deformation at each point. The micelles on the corners show some increased deformation suggesting soft polymer clusters. Areas of high deformation surrounding the nanocube are artifacts from the AFM tip dragging along the sidewalls. Some clusters of polymer are shown to be on the substrate in the bottom left and top right corners. (C) Snap-in map showing variation of the length of capillary snap-in across the surface. Areas expected to be micelle legs and thicker regions of the corona show larger snap-in values which could be attributed to thicker surface layers of stretched, swollen polymer. (D) Schematic showing regions of different curve behavior and number of curves in each region. The blue region corresponds to the corona and covers areas with a high confidence of being artifact free. Green regions are micelle bodies and are cut to reduce potential artifacts from the profile of the micelle. The yellow region is the "leg" region of the octopus micelles. The red circle is the center of the nanocube. Average and standard deviation values were calculated from these regions on the maps.

Information). Border regions were excluded due to potential artifacts, particularly for AFM tip dragging artifacts along the AgNC sidewall, as discussed earlier (section S.7 of the Supporting Information). In Figure 5A, the pull-off lengths of micelle bodies (13.7 \pm 2.0 nm, averages and standard deviations taken from the map in Figure 5A over the green region shown in Figure 5D) and the center of the AgNC face $(18.9 \pm 0.3 \text{ nm}, \text{ red region})$ are significantly shorter than the pull-off lengths in the region surrounding the micelles (22.0 \pm 1.5 nm, yellow region). This is consistent with the micelle body being a dense polymer cluster, and with increased bridging on the micelle legs consistent with a more lowdensity, extended polymer configuration. 51,57,63 Also worth noting is the extremely large pull-off lengths in the corona region of the AgNC, which is expected to be low density, radially outstretched polymer due to polymer-substrate interactions. 18 The pull-off map also shows that the pull-off lengths gradually decrease (i) in the leg regions, with distance from the micelle body, and (ii) in the corona, with distance away from the AgNC (roughly going from 80 to 20 nm). In Figure 5B, the edges and corners of the AgNC exhibit larger deformation than the center of the AgNC (average values of 0.8 ± 0.5 and 0.1 ± 0.1 nm, respectively), which is consistent with higher deformation for a thicker cluster of polymer

compared to a thin stretched layer of polymer (additional deformation images in section S.11 of the Supporting Information). We also observe a distinct difference in deformation values between the exact center of the micelle (0.8 \pm 0.2 nm) and the edges of the micelle (1.3 \pm 0.4 nm), which is likely due to either denser polymer packing in the micelle body center or lateral motion of the AFM tip or micelle. In Figure 5C, the snap-in exhibits higher values on the octopus micelle legs (6.5 \pm 1.3 nm) and lower values on the body (3.5 \pm 0.3 nm), consistent with legs being regions of lower polymer density and greater polymer swelling due to water vapor. Figure 5C also indicates that the snap-in length decreases gradually with distance away from the micelle center and away from the AgNC in the corona (roughly 40 to 3 nm).

Figure 6A shows a topographical visualization of the unperturbed, soft surface of the PEGylated AgNC calculated using the measured heights at $d_{\rm On}$, with the dashed lines corresponding to the line profiles shown in panels B-D of Figure 6. The d_{On} map can be thought of as the AgNC surface unperturbed by any AFM tip-sample interactions, assuming capillary necking is minimal. 52,54 In Figure 6B, a slight assymmetry in d_{On} height is noticeable due to the different sizes of the two cross-sectioned micelles. However, for both micelles, the d_{On} height is noticeably larger (e.g., in the center of the nanocube) than the profile given by the 6 nN height in the regions that are expected to be micelle legs. Furthermore, this structural feature is not observed for the $d_{\rm On}$ height profiles of PVP-grafted, shorter chain PEG-grafted AgNCs or PSgrafted AgNCs (Supporting Information, S2G) and suggests that it is not a capillary effect from topography.⁶⁴ In Figure 6C, this behavior is also observed in the corona, which is visible in the d_{On} height map as a large, raised ring of polymer that decays in height with distance away from the AgNC sidewalls. This decay for the d_{On} height is not observed in the 6 nN set point height profile, which simply shows the underlying flat substrate, with a flat cluster of likely physisorbed polymer stuck to the substrate near the outer rim of the corona. Furthermore, the space between the two AgNCs in Figure 6D shows a slight "U" shape to the d_{On} height profile that is consistent with polymer graft bridging between the AgNCs, in contrast with the flat substrate in the 6 nN height profile. Here we see that the polymer structure in this bridging region completely collapses (>40 nm) during AFM tip snap-in. These data demonstrate that the d_{On} height maps are capable of revealing the topographic profile of extreme low-density polymer areas that might not be fully captured using standard AFM tapping mode imaging.

CONCLUSION

To summarize, AFM topography and force volume mapping were used to characterize the nanoscale variation in polymer density and morphology at the surface of a single polymer-grafted AgNC. At sufficiently long chain lengths, the polymer grafts stretch toward high polymer density regions, forming octopus micelles on the AgNC edges and corners. Similar micelle formation was observed for both PEG and PS brushes, whereas native PVP grafts do not adopt a single grafting point brush conformation and do not segregate into the same micellar structure. For PEG, regions of high (micelle bodies) and low (micelle legs) polymer density could be quantitatively observed and delineated using force volume mapping. Furthermore, force mapping revealed the formation of a low density, swollen polymer corona extending away from the

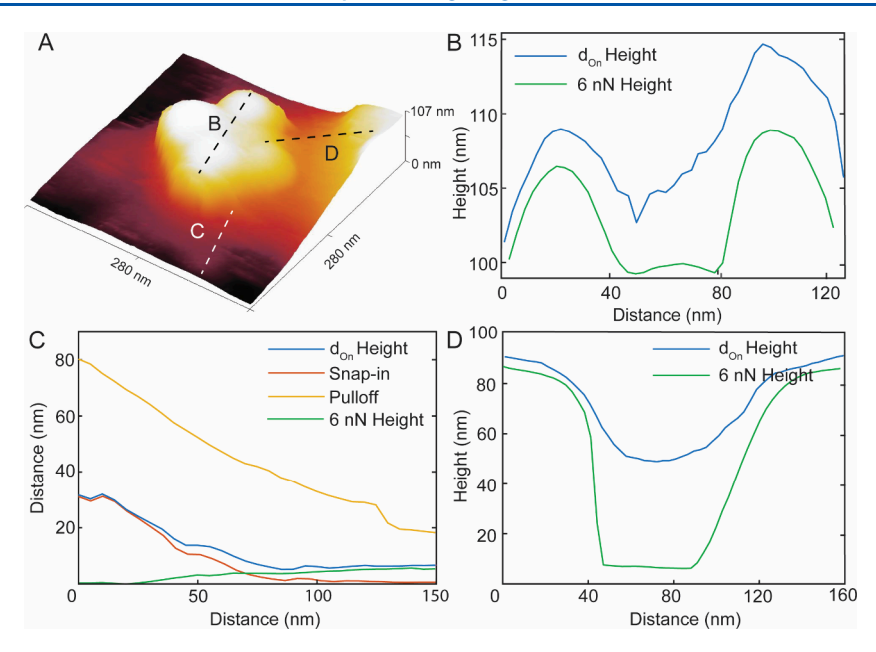


Figure 6. Visualization of the soft polymer structures. (A) 3D reconstructed topography image showing the height at $d_{\rm On}$ which should include any surface capillary layer or soft polymer structures that are disturbed after tip snap-in. (B) Cross section along line B in panel A. The $d_{\rm On}$ height shows wider structures on the insides of the raised micelle bodies. These structures are collapsed at the set point height of 6 nN. The height of this collapsed structure is mostly from the differences in snap-in distance across the surface and not from deformation during loading. (C) Cross section showing the corona profile starting from after the side wall artifacts. The $d_{\rm On}$ height gradually declines along with snap-in and pulloff length, while the 6 nN height shows a mostly flat substrate. (D) Cross section from line D shows the bridging between two nanocubes. The $d_{\rm On}$ height has a slight "U" curvature, while the 6 nN height shows a clear gap between the nanocubes with the flat substrate below. The bridging structure between the nanocube is disrupted by capillary snap-in.

AgNC and forming polymer bridges with other nearby AgNCs. To our knowledge, this is the first time that force volume mapping with this detail has been used to (i) image polymer grafts on a NP surface and (ii) to observe the differences in graft morphology within an octopus micelle. While this NP surface characterization provides a detailed map of polymer density contrast, the presence of a complex capillary layer that is in equilibrium with the solvent vapor/polymer environment limits the applicability of known analytical models for polymer brushes. Future directions for this work include carrying out force volume mapping studies for AgNCs and other NPs under different solvent/vapor conditions to be able to both validate and apply such analytical models.

METHODS

AgNC Preparation. AgNCs were synthesized using a polyol procedure published elsewhere. 45 AgNO₃ was reduced in a pentanediol, polyvinylpyrrolidone (PVP, $M_{\rm w} = 55\,000$) and CuCl₂ solution heated to a temperature of 195 °C. The reaction continued until the solution turned an orange-green color. After synthesis, 6 mL of ethanol and 2 mL of water was added to a concentrated solution of AgNCs in pentanediol before vacuum filtration. During vacuum filtration, Millipore Durapore membranes, with 0.65, 0.45, then 0.22 μ m pore sizes were used to separate any large particles from the AgNC dispersion. The solution was then concentrated by centrifugation at 2700 rpm for 60 min and redispersed in ethanol. For PEGylation, the AgNC solution was washed using centrifugation 3 times in deionized (DI) water (3400 rpm for 1 h). A PEG-thiol ($M_{\rm w}$ = 10 000) solution of 60 μ M was added to an AgNC solution in water with an optical density of 30 at $\lambda = 573$ nm. The PEGylated AgNC solution was continuously stirred for 48 h before being centrifuged an additional 3 times in water at 3500 rpm for 10 min. To transfer to chloroform, the PEGylated AgNC solution was centrifuged 3 times in methanol at 3000 rpm for 10 min. Chloroform was added and the sample was dispersed on an air-water interface. For the PS-grafted

AgNCs, ligand exchange and washing steps were performed in DMF. Washing was performed 8 times before dropcasting on a Si substrate.

AFM Characterization. A Park Systems NX20 atomic force microscope was used in PinPoint mode with a set point of 6 nN and an approach and retract rate of 10 μ m per second. Pixel numbers and scan dimensions were chosen to yield a pixel size roughly 3×3 nm². A 240AC-NA cantilever made by Mikromasch was used for force volume mapping measurements. AgNC samples were deposited on an air—water interface using established methods. 46,47 A silicon substrate was cleaned in freshly prepared piranha solution (5:3 ratio of sulfuric acid/hydrogen peroxide), washed in copious amounts of water and used to dipcoat the AgNC monolayer from the air water interface. Dipcoating was performed by quickly dipping the substrate into the monolayer with tweezers by hand. The resulting AgNCs on the substrate were dried in a vacuum desiccator for 2 h, rinsed for 1 min in DI water from a Milli-Q system (Thermo Fisher) then dried in a vacuum desiccator for an additional 2 h. The samples were allowed to equilibrium in the ambient environment of the testing facility with a humidity between 35 and 45% relative humidity (RH) for greater than 1 h before measurements began. Optical level sensitivity was calculated using another dry silicon substrate cleaned in piranha solution. The spring constant of the cantilever was calibrated with the Sader method before beginning the measurements. 65,66 All images were processed in Gwyddion (2.62) and leveled using 3-point leveling. Force volume maps were created using custom-made Python (3.10) and MATLAB (R2023a) scripts. Deformation and adhesion energy maps were calculated using the Park Systems SmartScan software (version RTM1). Average values and standard deviations given for each region were calculated from masks on the corresponding maps in Gwyddion. The individual curves shown in Figure 4 are randomly selected curves from each region that have representative morphology of the other curves from the region (Figure S8 of the Supporting Information). Tip deconvolution was conducted with a TipCheck sample made by Budget Sensors using blind reconstruction in Gwyddion (2.62).

ASSOCIATED CONTENT

Supporting Information

The Supporting Information is available free of charge at https://pubs.acs.org/doi/10.1021/acs.langmuir.4c01902.

Additional synthesis details, AFM data, and force volume maps (PDF)

AUTHOR INFORMATION

Corresponding Author

Authors

Wade Shipley — Materials Science and Engineering Program, University of California, San Diego, La Jolla, California 92023, United States

Yufei Wang – Materials Science and Engineering Program, University of California, San Diego, La Jolla, California 92023, United States

Joelle Chien — Aiiso Yufeng Li Family Department of Chemical and Nano Engineering, University of California, San Diego, La Jolla, California 92023-0448, United States; orcid.org/0009-0000-7561-4451

Bin Wang — Aiiso Yufeng Li Family Department of Chemical and Nano Engineering, University of California, San Diego, La Jolla, California 92023-0448, United States;
ocid.org/0000-0002-9373-5684

Complete contact information is available at: https://pubs.acs.org/10.1021/acs.langmuir.4c01902

Author Contributions

Conceptualization, Wade Shipley; methodology, Wade Shipley and Andrea R. Tao; investigation, Wade Shipley, Yufei Wang, Joelle Chien, and Bin Wang; visualization, Wade Shipley and Andrea R. Tao; funding, Andrea R. Tao; project administration, Andrea R. Tao; supervision, Andrea R. Tao; and writing, Wade Shipley and Andrea R. Tao.

Notes

The authors declare no competing financial interest.

ACKNOWLEDGMENTS

The authors acknowledge the use of facilities and instrumentation supported by the National Science Foundation through the University of California, San Diego Materials Research Science and Engineering Center (DMR-2011924). Wade Shipley acknowledges support from the Sloan Foundation and a Strategic Enhancement of Excellence through Diversity (SEED) fellowship. The authors thank Nano3 and the San Diego Nanotechnology Infrastructure (NSF Award ECCS-2025752).

REFERENCES

(1) Wong, C. K.; Chen, F.; Walther, A.; Stenzel, M. H. Bioactive Patchy Nanoparticles with Compartmentalized Cargoes for Simultaneous and Trackable Delivery. *Angew. Chem.* **2019**, *131* (22), 7413–7418.

- (2) Kim, C. K.; Ghosh, P.; Rotello, V. M. Multimodal Drug Delivery Using Gold Nanoparticles. *Nanoscale* **2009**, *1* (1), 61–67.
- (3) Tran, L. T. C.; Lesieur, S.; Faivre, V. Janus Nanoparticles: Materials, Preparation and Recent Advances in Drug Delivery. *Expert opinion on drug delivery* **2014**, *11* (7), 1061–1074.
- (4) Jin, C.; Qu, Y.; Wang, M.; Han, J.; Hu, Y.; Guo, R. Aqueous Solution-Based Fe3O4 Seed-Mediated Route to Hydrophilic Fe3O4-Au Janus Nanoparticles. *Langmuir* **2016**, 32 (18), 4595–4601.
- (5) Li, L.; Chen, B.; Guo, M.; Yang, Q.; Zhang, Y.; Zhang, M. Platinum Janus Nanoparticles as Peroxidase Mimics for Catalytic Immunosorbent Assay. *ACS Appl. Nano Mater.* **2022**, *5* (1), 1397–1407.
- (6) Choueiri, R. M.; Galati, E.; Klinkova, A.; Thérien-Aubin, H.; Kumacheva, E. Linear Assembly of Patchy and Non-Patchy Nanoparticles. *Faraday Discuss.* **2016**, *191*, 189–204.
- (7) Roberts, C. J.; Blanco, M. A. Role of Anisotropic Interactions for Proteins and Patchy Nanoparticles. *J. Phys. Chem. B* **2014**, *118* (44), 12599–12611.
- (8) Lunn, D. J.; Finnegan, J. R.; Manners, I. Self-Assembly of "Patchy" Nanoparticles: A Versatile Approach to Functional Hierarchical Materials. *Chem. Sci.* **2015**, 6 (7), 3663–3673.
- (9) Duan, H.; Malesky, T.; Wang, J.; Liu, C. H.; Tan, H.; Nieh, M. P.; Lin, Y.; He, J. Patchy Metal Nanoparticles with Polymers: Controllable Growth and Two-Way Self-Assembly. *Nanoscale* **2022**, *14* (19), 7364–7371.
- (10) Wu, B.; Liu, D.; Mubeen, S.; Chuong, T. T.; Moskovits, M.; Stucky, G. D. Anisotropic Growth of TiO2 onto Gold Nanorods for Plasmon-Enhanced Hydrogen Production from Water Reduction. *J. Am. Chem. Soc.* **2016**, *138* (4), 1114–1117.
- (11) Zhou, J.; Creyer, M. N.; Chen, A.; Yim, W.; Lafleur, R. P. M.; He, T.; Lin, Z.; Xu, M.; Abbasi, P.; Wu, J.; Pascal, T. A.; Caruso, F.; Jokerst, J. V. Stereoselective Growth of Small Molecule Patches on Nanoparticles. *J. Am. Chem. Soc.* **2021**, *143* (31), 12138–12144.
- (12) Şologan, M.; Marson, D.; Polizzi, S.; Pengo, P.; Boccardo, S.; Pricl, S.; Posocco, P.; Pasquato, L. Patchy and Janus Nanoparticles by Self-Organization of Mixtures of Fluorinated and Hydrogenated Alkanethiolates on the Surface of a Gold Core. *ACS Nano* **2016**, *10* (10), 9316–9325.
- (13) Rossner, C.; Tang, Q.; Müller, M.; Kothleitner, G. Phase Separation in Mixed Polymer Brushes on Nanoparticle Surfaces Enables the Generation of Anisotropic Nanoarchitectures. *Soft Matter* **2018**, *14* (22), 4551–4557.
- (14) Galati, E.; Tao, H.; Rossner, C.; Zhulina, E. B.; Kumacheva, E. Morphological Transitions in Patchy Nanoparticles. *ACS Nano* **2020**, *14* (4), 4577–4584.
- (15) Kim, A.; Zhou, S.; Yao, L.; Ni, S.; Luo, B.; Sing, C. E.; Chen, Q. Tip-Patched Nanoprisms from Formation of Ligand Islands. *J. Am. Chem. Soc.* **2019**, *141* (30), 11796–11800.
- (16) Choueiri, R. M.; Galati, E.; Thérien-Aubin, H.; Klinkova, A.; Larin, E. M.; Querejeta-Fernández, A.; Han, L.; Xin, H. L.; Gang, O.; Zhulina, E. B.; Rubinstein, M.; Kumacheva, E. Surface Patterning of Nanoparticles with Polymer Patches. *Nature* **2016**, 538 (7623), 79–83
- (17) Galati, E.; Tebbe, M.; Querejeta-Fernández, A.; Xin, H. L.; Gang, O.; Zhulina, E. B.; Kumacheva, E. Shape-Specific Patterning of Polymer-Functionalized Nanoparticles. *ACS Nano* **2017**, *11* (5), 4995–5002.
- (18) Yu, L.; Zhang, N.; Zhang, N. N.; Gu, Q.; Xue, Y.; Wang, Y. X.; Han, C. L.; Liu, K.; Sun, Z. Y.; Qian, H. J.; Lu, Z. Y. Solvent-Evaporation Induced and Mechanistic Entropy-Enthalpy-Balance Controlled Polymer Patch Formation on Nanoparticle Surfaces. *J. Phys. Chem. Lett.* **2021**, *12* (30), 7100–7105.
- (19) Choi, B. C.; Choi, S.; Leckband, D. E. Poly(N-Isopropyl Acrylamide) Brush Topography: Dependence on Grafting Conditions and Temperature. *Langmuir* **2013**, 29 (19), 5841–5850.
- (20) Williams, D. R. M. Grafted Polymers in Bad Solvents: Octopus Surface Micelles. *J. Phys. II* **1993**, *3* (9), 1313–1318.
- (21) Stamouli, A.; Pelletier, E.; Koutsos, V.; van der Vegte, E.; Hadziioannou, G. An Atomic Force Microscopy Study on the

- Transition from Mushrooms to Octopus Surface "Micelles" by Changing the Solvent Quality. *Langmuir* 1996, 12 (13), 3221–3224.
- (22) Zhulina, E.; Balazs, A. C. Designing Patterned Surfaces by Grafting Y-Shaped Copolymers. *Macromolecules* **1996**, 29 (7), 2667–2673.
- (23) Yeung, C.; Balazs, A. C.; Jasnow, D. Lateral Instabilities in a Grafted Layer in a Poor Solvent. *Macromolecules* **1993**, 26 (8), 1914–1921.
- (24) Singh, C.; Zhulina, E. B.; Gersappe, D.; Pickett, G. T.; Balazs, A. C. A "Jumping Micelle" Phase Transition. *Macromolecules* **1996**, 29 (23), 7637–7640.
- (25) Nnebe, I. M.; Schneider, J. W. A Tapping-Mode AFM Study of the Compression of Grafted Poly(Ethylene Glycol) Chains. *Macromolecules* **2006**, 39 (10), 3616–3621.
- (26) Tuermer-Lee, J. X.; Lim, A.; Ah, L.; Blau, R.; Qie, Y.; Shipley, W.; Kayser, L. V.; Russman, S. M.; Tao, A. R.; Dayeh, S. A.; Lipomi, D. J. Synthesis of PEDOT:PSS Brushes Grafted from Gold Using ATRP for Increased Electrochemical and Mechanical Stability. ACS Macro Lett. 2023, 12 (12), 1718–1726.
- (27) Stan, G.; Delrio, F. W.; MacCuspie, R. I.; Cook, R. F. Nanomechanical Properties of Polyethylene Glycol Brushes on Gold Substrates. *J. Phys. Chem. B* **2012**, *116* (10), 3138–3147.
- (28) Huang, Q.; Yoon, I.; Villanueva, J.; Kim, K.; Sirbuly, D. J. Quantitative Mechanical Analysis of Thin Compressible Polymer Monolayers on Oxide Surfaces. *Soft Matter* **2014**, *10* (40), 8001–8010
- (29) Sui, X.; Zapotoczny, S.; Benetti, E. M.; Schön, P.; Vancso, G. J. Characterization and Molecular Engineering of Surface-Grafted Polymer Brushes across the Length Scales by Atomic Force Microscopy. *J. Mater. Chem.* **2010**, 20 (24), 4981–4993.
- (30) Kutnyanszky, E.; Vancso, G. J. Nanomechanical Properties of Polymer Brushes by Colloidal AFM Probes. *Eur. Polym. J.* **2012**, 48 (1), 8–15.
- (31) Hentschel, C.; Wagner, H.; Smiatek, J.; Heuer, A.; Fuchs, H.; Zhang, X.; Studer, A.; Chi, L. AFM-Based Force Spectroscopy on Polystyrene Brushes: Effect of Brush Thickness on Protein Adsorption. *Langmuir* **2013**, 29 (6), 1850–1856.
- (32) Tranchida, D.; Sperotto, E.; Chateauminois, A.; Schönherr, H. Entropic Effects on the Mechanical Behavior of Dry Polymer Brushes During Nanoindentation by Atomic Force Microscopy. *Macromolecules* **2011**, *44* (2), 368–374.
- (33) Dokukin, M. E.; Kuroki, H.; Minko, S.; Sokolov, I. AFM Study of Polymer Brush Grafted to Deformable Surfaces: Quantitative Properties of the Brush and Substrate Mechanics. *Macromolecules* **2017**, *50* (1), 275–282.
- (34) Goodman, D.; Kizhakkedathu, J. N.; Brooks, D. E. Evaluation of an Atomic Force Microscopy Pull-off Method for Measuring Molecular Weight and Polydispersity of Polymer Brushes: Effect of Grafting Density. *Langmuir* **2004**, *20* (15), 6238–6245.
- (35) Yang, P.; Song, Y.; Feng, W.; Zhang, W. Unfolding of a Single Polymer Chain from the Single Crystal by Air-Phase Single-Molecule Force Spectroscopy: Toward Better Force Precision and More Accurate Description of Molecular Behaviors. *Macromolecules* **2018**, *51* (18), 7052–7060.
- (36) Ma, Z.; Yang, P.; Zhang, X.; Jiang, K.; Song, Y.; Zhang, W. Quantifying the Chain Folding in Polymer Single Crystals by Single-Molecule Force Spectroscopy. *ACS Macro Lett.* **2019**, 8 (9), 1194–1199.
- (37) Song, Y.; Ma, Z.; Yang, P.; Zhang, X.; Lyu, X.; Jiang, K.; Zhang, W. Single-Molecule Force Spectroscopy Study on Force-Induced Melting in Polymer Single Crystals: The Chain Conformation Matters. *Macromolecules* **2019**, *52* (3), 1327–1333.
- (38) Lemoine, P.; Dooley, C.; Morelli, A.; Harrison, E.; Dixon, D. AFM Study of Organic Ligand Packing on Gold for Nanoparticle Drug Delivery Applications. *Appl. Surf. Sci.* **2022**, *574*, 151386.
- (39) Dokukin, M. E.; Sokolov, I. Nanoscale Compositional Mapping of Cells, Tissues, and Polymers with Ringing Mode of Atomic Force Microscopy. *Sci. Rep.* **2017**, *7* (1), 1–11.

- (40) Olubowale, O. H.; Biswas, S.; Azom, G.; Prather, B. L.; Owoso, S. D.; Rinee, K. C.; Marroquin, K.; Gates, K. A.; Chambers, M. B.; Xu, A.; Garno, J. C. May the Force Be with You!" Force-Volume Mapping with Atomic Force Microscopy. *ACS Omega* **2021**, *6* (40), 25860–25875
- (41) Dufrêne, Y. F.; Martínez-Martín, D.; Medalsy, I.; Alsteens, D.; Müller, D. J. Multiparametric Imaging of Biological Systems by Force-Distance Curve-Based AFM. *Nat. Methods* **2013**, *10* (9), 847–854.
- (42) Szekrényes, D. P.; Pothorszky, S.; Zámbó, D.; Osváth, Z.; Deák, A. Investigation of Patchiness on Tip-Selectively Surface-Modified Gold Nanorods. *J. Phys. Chem. C* **2018**, *122* (3), 1706–1710.
- (43) Choi, M. H.; Jeong, S.; Wang, Y.; Cho, S. J.; Park, S. I.; Ye, X.; Baker, L. A. Characterization of Ligand Adsorption at Individual Gold Nanocubes. *Langmuir* **2021**, *37* (25), 7701–7711.
- (44) Gao, B.; Arya, G.; Tao, A. R. Self-Orienting Nanocubes for the Assembly of Plasmonic Nanojunctions. *Nat. Nanotechnol.* **2012**, *7* (7), 433–437
- (45) Sun, Y.; Xia, Y. Shape-Controlled Synthesis of Gold and Silver Nanoparticles. *Science* **2002**, 298 (5601), 2176–2179.
- (46) Zeng, Y.; Qian, H.; Rozin, M. J.; Liu, Z.; Tao, A. R. Enhanced Second Harmonic Generation in Double-Resonance Colloidal Metasurfaces. *Adv. Funct. Mater.* **2018**, 28 (51), 1803019.
- (47) Zeng, Y.; Ananth, R.; Dill, T. J.; Rodarte, A.; Rozin, M. J.; Bradshaw, N.; Brown, E. R.; Tao, A. R. Metasurface-Enhanced Raman Spectroscopy (mSERS) for Oriented Molecular Sensing. *ACS Appl. Mater. Interfaces* **2022**, *14* (28), 32598–32607.
- (48) Xia, X.; Yang, M.; Wang, Y.; Zheng, Y.; Li, Q.; Chen, J.; Xia, Y. Quantifying the Coverage Density of Poly(Ethylene Glycol) Chains on the Surface of Gold Nanostructures. ACS Nano 2012, 6 (1), 512–522.
- (49) Chang, W.-C.; Tai, J.-T.; Wang, H.-F.; Ho, R.-M.; Hsiao, T.-C.; Tsai, D.-H. Surface PEGylation of Silver Nanoparticles: Kinetics of Simultaneous Surface Dissolution and Molecular Desorption. *Langmuir* **2016**, *32* (38), 9807–9815.
- (50) Halperin, A.; Zhulina, E. B. Stretching Polymer Brushes in Poor Solvents. *Macromolecules* **1991**, 24 (19), 5393–5397.
- (51) Zhulina, E.; Walker, G. C.; Balazs, A. C. Modeling the Interactions between Atomic Force Microscope Tips and Polymeric Substrates. *Langmuir* 1998, 14 (16), 4615–4622.
- (52) Döppenschmidt, A.; Butt, H. J. Measuring the Thickness of the Liquid-like Layer on Ice Surfaces with Atomic Force Microscopy. *Langmuir* **2000**, *16* (16), 6709–6714.
- (53) Xiao, X.; Qian, L. Investigation of Humidity-Dependent Capillary Force. *Langmuir* **2000**, *16* (21), 8153–8158.
- (54) Sudersan, P.; Müller, M.; Hormozi, M.; Li, S.; Butt, H.-J.; Kappl, M. Method to Measure Surface Tension of Microdroplets Using Standard AFM Cantilever Tips. *Langmuir* **2023**, 39 (30), 10367–10374.
- (55) Uhlig, M. R.; Magerle, R. Unraveling Capillary Interaction and Viscoelastic Response in Atomic Force Microscopy of Hydrated Collagen Fibrils. *Nanoscale* **2017**, *9* (3), 1244–1256.
- (56) Barcons, V.; Verdaguer, A.; Font, J.; Chiesa, M.; Santos, S. Nanoscale Capillary Interactions in Dynamic Atomic Force Microscopy. J. Phys. Chem. C 2012, 116 (14), 7757–7766.
- (57) Goodman, D.; Kizhakkedathu, J. N.; Brooks, D. E. Attractive Bridging Interactions in Dense Polymer Brushes in Good Solvent Measured by Atomic Force Microscopy. *Langmuir* **2004**, 20 (6), 2333–2340.
- (58) Zlatanova, J.; Lindsay, S. M.; Leuba, S. H. Single Molecule Force Spectroscopy in Biology Using the Atomic Force Microscope. *Prog. Biophys. Mol. Biol.* **2000**, 74 (1–2), 37–61.
- (59) Ritsema Van Eck, G. C.; Veldscholte, L. B.; Nijkamp, J. H. W. H.; De Beer, S. Sorption Characteristics of Polymer Brushes in Equilibrium with Solvent Vapors. *Macromolecules* **2020**, *53* (19), 8428–8437
- (60) Galvin, C. J.; Genzer, J. Swelling of Hydrophilic Polymer Brushes by Water and Alcohol Vapors. *Macromolecules* **2016**, 49 (11), 4316–4329.

- (61) Ritsema van Eck, G. C.; Chiappisi, L.; de Beer, S. Fundamentals and Applications of Polymer Brushes in Air. *ACS Appl. Polym. Mater.* **2022**, *4* (5), 3062–3087.
- (62) Melzak, K. A.; Moreno-Flores, S.; Yu, K.; Kizhakkedathu, J.; Toca-Herrera, J. L. Rationalized Approach to the Determination of Contact Point in Force–Distance Curves: Application to Polymer Brushes in Salt Solutions and in Water. *Microsc. Res. Technol.* **2010**, 73 (10), 959–964.
- (63) Hamilton-Brown, P.; Gengenbach, T.; Griesser, H. J.; Meagher, L. End Terminal, Poly(Ethylene Oxide) Graft Layers: Surface Forces and Protein Adsorption. *Langmuir* **2009**, 25 (16), 9149–9156.
- (64) Sirghi, L.; Nakagiri, N.; Sugisaki, K.; Sugimura, H.; Takai, O. Effect of Sample Topography on Adhesive Force in Atomic Force Spectroscopy Measurements in Air. *Langmuir* **2000**, *16* (20), 7796–7800.
- (65) Sader, J. E.; Larson, I.; Mulvaney, P.; White, L. R. Method for the Calibration of Atomic Force Microscope Cantilevers. *Rev. Sci. Instrum.* **1995**, *66* (7), 3789–3798.
- (66) Sader, J. E.; Borgani, R.; Gibson, C. T.; Haviland, D. B.; Higgins, M. J.; Kilpatrick, J. I.; Lu, J.; Mulvaney, P.; Shearer, C. J.; Slattery, A. D.; Thorén, P.-A.; Tran, J.; Zhang, H.; Zhang, H.; Zheng, T. A Virtual Instrument to Standardise the Calibration of Atomic Force Microscope Cantilevers. *Rev. Sci. Instrum.* **2016**, 87 (9), 93711.